

MAE263F Project Final Report

Ryman Wong, Jens Dekker

I. INTRODUCTION

Robot manipulation has long been dominated by rigid-link manipulators that achieve high precision and repeatability in structured environments such as manufacturing and assembly lines. These systems rely on well-defined kinematic and dynamic models to perform tasks with millimeter-level accuracy. However, their rigidity becomes a limitation in unstructured or dynamic environments, particularly where interaction with delicate or irregular objects is required. In contrast, soft robotic manipulators, composed of highly deformable materials such as silicone or elastomers, can passively adapt their shape to external forces, allowing for safer and more flexible interaction. The study of soft manipulators remains an ongoing research topic due to several challenges, such as difficulty of achieving accurate sensing and control for unknown environment. Despite these challenges, soft robotic manipulation has demonstrated promising applications in diverse fields such as minimally invasive surgery, agricultural harvesting, and marine exploration, where adaptability and gentle contact are paramount.

II. MOTIVATION

This project focuses on developing and simulating a soft robotic manipulator for underwater exploration, mounted in front of a submarine. The manipulator will perform tasks such as environmental monitoring, sample collection, and interaction with fragile marine organisms like corals or sponges. Traditional rigid arms are limited in such settings due to their inability to safely contact or adapt to irregular surfaces and their sensitivity to hydrodynamic disturbances. In contrast, a soft manipulator's compliance allows it to absorb fluid-induced forces and conform to its surroundings, making it inherently safer and more stable for trajectory tracking under uncertainty. The use of soft manipulators in underwater exploration could significantly enhance the precision and safety of data collection and specimen sampling, contributing to sustainable ocean research and reducing ecological damage during exploration missions.

The proposed system consists of a soft robotic manipulator mounted on a submarine, designed to maintain its end-effector position while the vehicle is stationary. Hydrodynamic forces generated by the flow field act on the manipulator, causing deformation and positional drift. The control objective is to maintain the desired end-effector position by actively adjusting the base of the robot connected to the vehicle, similar to

an inverted pendulum stabilization problem. The manipulator operates in an uncertain underwater environment affected by random disturbances such as local flow turbulence, gusts, and collisions with small obstacles. This setup represents a complex nonlinear control problem where the compliant structure must counteract fluid-induced motion while preserving trajectory stability and precision. Addressing these challenges requires accurate modeling of both the manipulator's elasticity and the external flow dynamics, as well as a robust control strategy capable of compensating for continuous disturbances.

III. LITERATURE REVIEW

Control of a soft robotic appendage is a well-studied challenge, with multiple simulation approaches developed to predict motion under external forces and control inputs. There is a model of a soft appendage using a planar discrete elastic rod to analyze its swinging motion around a fixed point [1]. The hybrid control design used separate controllers for upward equilibrium stabilization and for driving the appendage back into position. While the model operated in air and ignored fluid dynamics, the control strategy offers valuable insights for stabilization in dynamic environments. The present project extends this concept into an underwater setting, where hydrodynamic forces dominate. Instead of stabilizing a static equilibrium, the goal is to maintain the end-effector position under continuous flow disturbances, emphasizing continuous feedback control rather than hybrid switching.

Similarly, another model used a planar discrete elastic rod to simulate eel-like underwater locomotion [2]. This work introduced internal damping and explored various hydrodynamic modeling approaches but assumed a stationary fluid. In contrast, the proposed system will operate within time-varying ocean currents, requiring stabilization under external flow disturbances. Although this study focuses on locomotion rather than manipulation, it provides useful insights into underwater dynamics and the impact of fluid-structure interactions, which are directly applicable to the proposed underwater manipulator.

Many applications propose utilizing pneumatic or hydraulic actuation for controlling the robot to take advantage of the soft links [3] [4]. This will lead to novel actuation methods for the robot where each node in a discrete elastic rod model can be actuated. This leads to an extension where the proposed study can look at the effects of disturbances on a manipulator in motion.

In the most fascinating paper, a neural controller can be used to abstract the minutiae of a control algorithm [5]. The main model used will still be a discrete elastic rod in a

manner similar to that proposed in the paper. Combining the novel actuation methods presented in previous papers with the control optimization methods for deformable linear objects in this paper, there can be an extension looking into integrating a neural control scheme to have the appendage move to a target location under load.

IV. METHODOLOGY

A. Rod Properties

The soft robotic manipulator is modeled as a planar discrete elastic rod (DER) consisting of 19 nodes, corresponding to 18 segments with a total rod length of 1 m. Each node has a circular cross-sectional radius of 0.05 m. The rod is constructed as a composite structure composed of an outer EcoFlex 00–30 silicone layer and an inner thermoplastic polyurethane (TPU) reinforcement layer. This design provides improved axial stability while retaining the high compliance required for soft robotic manipulation [6].

EcoFlex 00–30 was selected as the primary material due to its mechanical similarity to human soft tissue and its widespread use in soft robotic applications [6] [7].

The density is calculated from the specified specific gravity provided in the datasheet:

$$\rho_{\text{silicone}} = 1.07 \times 1000 = 1070 \text{ kg/m}^3$$

Since the manufacturer datasheet does not provide a direct Young's modulus, an approximation is made using the reported 100% modulus of 10 psi, yielding:

$$E_{\text{silicone}} = 10 \text{ psi} = 68.95 \text{ kPa}$$

The TPU chosen for this is the Ultrafuse TPU 95A and from the data sheet, its material properties are [8]:

$$\rho_{\text{TPU}} = 1149 \text{ kg/m}^3 \quad E_{\text{TPU}} = 48.4 \text{ MPa}$$

The rod's cross-section consists of an outer silicone annulus of thickness 0.03 m and an inner TPU annulus of thickness 0.01 m, with a small hollow core at the center. Because the two materials are concentric and share a common centroid, their stiffness contributions can be superposed.

For a hollow circular region with outer radius R_o and inner radius R_i , the cross-sectional area and second moment of area are:

$$A = \pi (R_o^2 - R_i^2) \quad I = \frac{\pi}{4} (R_o^4 - R_i^4)$$

Let A_{sil} , A_{TPU} denote the areas of the silicone and TPU regions, and I_{sil} , I_{TPU} their corresponding second moments of area.

The composite axial stiffness and bending stiffness are then obtained by summing the contributions of each material:

$$EA = E_{\text{sil}} A_{\text{sil}} + E_{\text{TPU}} A_{\text{TPU}} \quad (1)$$

$$EI = E_{\text{sil}} I_{\text{sil}} + E_{\text{TPU}} I_{\text{TPU}} \quad (2)$$

Here, EA governs the rod's resistance to stretching and compression, while EI governs resistance to curvature.

B. Simulation Environment

1) *Implicit Euler Method*: The dynamic equations of the discrete elastic rod are integrated in time using an implicit Euler method. This approach is chosen due to its unconditional stability when simulating stiff elastic systems subject to large deformations and nonlinear hydrodynamic forces.

Let $\mathbf{q}_n \in \mathbb{R}^{2N}$ and $\mathbf{u}_n \in \mathbb{R}^{2N}$ denote the nodal positions and velocities at time step n , respectively, and let Δt denote the time step size. Under the implicit Euler formulation, the velocity and acceleration updates are given by

$$\mathbf{u}_{n+1} = \frac{\mathbf{q}_{n+1} - \mathbf{q}_n}{\Delta t} \quad (3)$$

Substituting these expressions into Newton's second law yields a nonlinear residual equation in terms of the unknown configuration \mathbf{q}_{n+1} :

$$\mathbf{f} = \mathbf{F}_{\text{inertia}} - \mathbf{F}_{\text{elastic}} - \mathbf{F}_v - \mathbf{W} - \mathbf{F}_h \quad (4)$$

where \mathbf{f} denotes the force residual evaluated at the unknown configuration \mathbf{q}_{n+1} .

The inertial force term arises from the implicit Euler discretization of the acceleration and is given by:

$$\mathbf{F}_{\text{inertia}} = \mathbf{M} \left(\frac{\mathbf{q}_{n+1} - \mathbf{q}_n}{\Delta t^2} - \frac{\mathbf{u}_n}{\Delta t} \right) \quad (5)$$

where \mathbf{M} is the lumped mass matrix and \mathbf{u}_n is the velocity at the previous time step.

The elastic force consists of stretching and bending contributions:

$$\mathbf{F}_{\text{elastic}} = \mathbf{F}_{\text{stretch}} + \mathbf{F}_{\text{bend}} \quad (6)$$

which are computed from the discrete elastic rod formulation using the axial stiffness EA and bending stiffness EI .

Structural damping is modeled as a velocity-proportional force,

$$\mathbf{F}_v = -\mathbf{C}\mathbf{u}_{n+1} = -\mathbf{C} \frac{\mathbf{q}_{n+1} - \mathbf{q}_n}{\Delta t}, \quad (7)$$

where \mathbf{C} is a diagonal damping matrix representing material and numerical dissipation. In this work, the damping matrix is constructed on a per-node basis using a Stokes-type drag approximation, such that the translational damping coefficients along both the x - and y -directions for each node are given by

$$C_{2k,2k} = C_{2k+1,2k+1} = 6\pi\nu r_{out}, \quad (8)$$

where r_{out} is the total rod radius and ν denotes the dynamic viscosity of the surrounding fluid. For all simulations, the viscosity is assumed to be that of seawater and is set to $\mu = 1 \times 10^{-3}$ Pas [9].

The hydrodynamic force \mathbf{F}_h accounts for fluid–structure interaction and is evaluated using a either low-Reynolds-number or high-Reynolds-number quadratic drag model based on the relative velocity between the rod and the background flow,

$$\mathbf{F}_h = \mathbf{F}_{\text{hydro}}(\mathbf{q}_{n+1}, \mathbf{u}_{n+1}, \mathbf{u}_f) \quad (9)$$

where \mathbf{u}_f denotes the background fluid velocity field. This will be further elaborated in Section IV-C.

The term \mathbf{W} represents external body forces. Since the simulation is restricted to the xy -plane and gravitational acceleration acts in the out-of-plane ($-z$) direction and therefore does not influence the in-plane dynamics of the rod. As a result, gravitational effects are neglected in this study.

Since the residual equation is nonlinear in \mathbf{q}_{n+1} , it is solved using a Newton–Raphson iteration. At each iteration, the residual vector \mathbf{f} is evaluated at the current configuration and linearized using its Jacobian \mathbf{J} . The resulting linear system

$$\mathbf{J} \delta \mathbf{q} = \mathbf{f} \quad (10)$$

is solved for the position increment $\delta \mathbf{q}$, where only unconstrained degrees of freedom are included.

The configuration is then updated according to:

$$\mathbf{q}_{n+1}^{(k+1)} = \mathbf{q}_{n+1}^{(k)} - \delta \mathbf{q} \quad (11)$$

Iterations continue until the norm of the residual falls below a prescribed tolerance or a maximum number of iterations is reached.

The Jacobian matrix is given by:

$$\mathbf{J} = \frac{\mathbf{M}}{\Delta t^2} - \frac{\partial \mathbf{F}_{\text{elastic}}}{\partial \mathbf{q}} - \frac{\partial \mathbf{F}_{\text{damp}}}{\partial \mathbf{q}} - \frac{\partial \mathbf{F}_{\text{hydro}}}{\partial \mathbf{q}} \quad (12)$$

Only unconstrained degrees of freedom are included in the Newton–Raphson solve, while fixed boundary conditions are enforced by excluding constrained indices from the linear system. In this simulation, the first node is fully clamped, with both its x - and y -coordinates fixed. Additionally, the x -coordinate of the second node is constrained to prevent rigid-body rotation while allowing vertical motion. All remaining degrees of freedom are treated as free and are updated during the Newton iteration.

Iterations proceed until the norm of the residual falls below a prescribed tolerance, defined as:

$$\text{tol} = \frac{EI}{L_{\text{rod}}^2} \times 10^{-3}, \quad (13)$$

where L_{rod} denotes the total length of the rod. If convergence is not achieved within a specified maximum number of iterations, the solver terminates and the time step is rejected.

Upon convergence, the updated configuration \mathbf{q}_{n+1} is accepted, completing the implicit Euler time step.

2) Controller Design: To actuate the soft robotic manipulator and regulate its motion, a proportional–integral–derivative (PID) controller is applied at the base of the rod. Control input is applied to the y -coordinate of the first node, which serves as the actuation point for the entire structure. By vertically displacing the base, the rod deforms elastically and the position of the end node is controlled to track a desired target position.

The control objective is defined in terms of the end-node position error along the y -direction, which is represented as:

$$e_y(t) = y_{\text{des}}(t) - y_{\text{end}}(t) \quad (14)$$

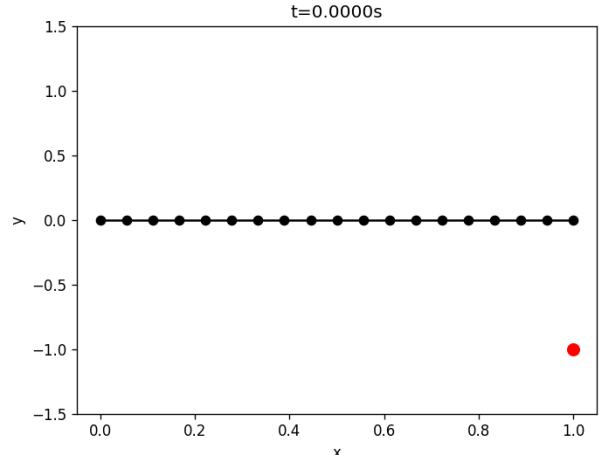


Fig. 1: Initial Setup of Simulation

where y_{des} denotes the desired vertical position and y_{end} is the vertical position of the last node of the rod.

The PID control law governing the base motion is given by:

$$\dot{y}_c(t) = K_p e_y(t) + K_i \int_0^t e_y(\tau) d\tau + K_d \frac{de_y(t)}{dt} \quad (15)$$

where K_p , K_i , and K_d are the proportional, integral, and derivative gains respectively.

The commanded base position is then obtained by time integration,

$$y_c(t + \Delta t) = y_c(t) + \dot{y}_c(t) \Delta t \quad (16)$$

In addition to controlling the y position of the base node, the y -coordinate of the second node is also constrained to regulate the local base orientation of the rod. This is enforced by prescribing the second node position as:

$$q_1^y = y_c + \Delta L \sin(\theta) \quad (17)$$

where y_c is the controlled base displacement and θ is the instantaneous rod orientation computed from the terminal segment using:

$$\theta = \arctan 2(y_1 - y_0, x_1 - x_0) \quad (18)$$

This additional constraint suppresses excessive local rotation at the base, removes rigid-body modes, and helps preserve the structural integrity of the rod during large deformations and under strong hydrodynamic loading.

As only the vertical motion of the base node is actively controlled in this framework, any axial compression or extension of the rod induced by hydrodynamic forces or elastic deformation cannot be directly regulated by the controller.

As a result, the PID controller influences the rod shape and end-effector position solely through vertical base displacement, relying on the rod's elastic response to propagate motion along its length.

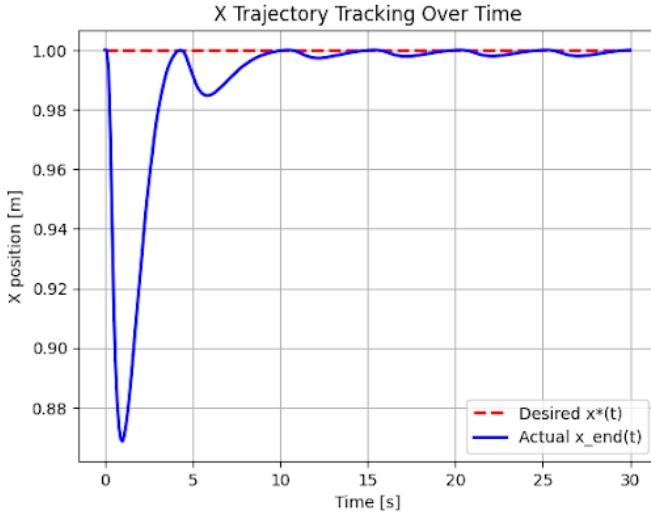


Fig. 2: x trajectory no hydrodynamic forces

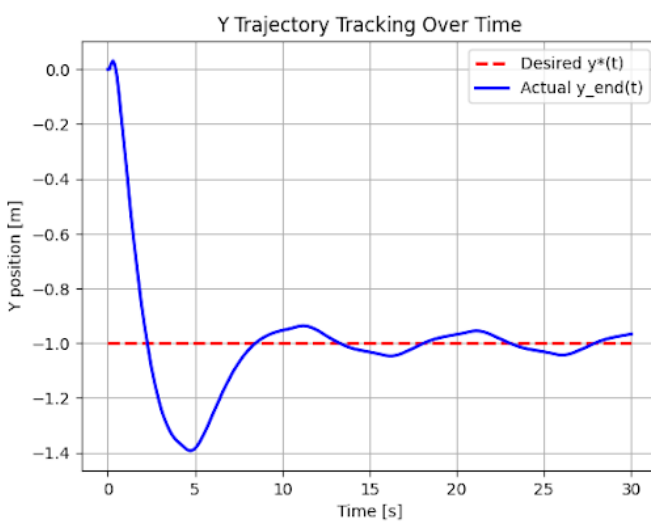


Fig. 3: y trajectory no hydrodynamic forces

3) *No Load Testing:* To verify the implementation of the simulation environment and the effectiveness of the controller in isolation, a no-load test is first conducted without hydrodynamic forces. In this configuration, the rod dynamics are solely governed by inertia, elastic deformation, and viscous damping. This test serves as a baseline validation of the numerical solver, boundary conditions, and controller implementation.

To evaluate the no-load condition, the rod is initially placed at rest with the first node positioned at the origin $(0, 0)$. The initial configuration of the system is illustrated in Figure 1, where the red marker denotes the desired target position. In this example, the target is set to $(1, -1)$ to observe the rod's natural deformation and transient response as it is actuated by the base controller in a viscous environment without external loading.

The results of the position tracking tests are presented in

Figures 2 and 3, which show the appendage tip trajectories in the X - and Y -directions against time. Both plots indicate that the PID controller is able to guide the soft rod toward the desired target location with stable convergence and minimal overshoot.

C. Hydrodynamic Modeling

With the simulation framework and controller validated under no-load conditions, hydrodynamic forces are introduced to provide a more realistic representation of underwater operation. Two flow regimes are considered: low Reynolds number and high Reynolds number environments. This distinction allows the model to capture both viscous-dominated and inertia-dominated fluid–structure interactions commonly encountered by soft robotic manipulators in water. In addition, transient flow disturbances are introduced in the form of gusts to evaluate the robustness of the rod dynamics and control strategy under unsteady hydrodynamic loading.

1) *Low Reynolds Number Environment:* In the low Reynolds number regime, viscous effects dominate and inertial contributions from the surrounding fluid are negligible. Under this assumption, hydrodynamic forces are modeled using Resistive Force Theory (RFT), where the drag force at each node is linearly proportional to the relative velocity between the rod and the background flow.

The nodal velocity is computed as [10]:

$$\mathbf{u}_k = \frac{\mathbf{x}_k^{n+1} - \mathbf{x}_k^n}{\Delta t} \quad (19)$$

and the relative velocity is given by:

$$\mathbf{u}_{\text{rel},k} = \mathbf{u}_k - \mathbf{u}_f \quad (20)$$

where \mathbf{u}_f denotes the background fluid velocity.

The local rod tangent direction \mathbf{t}_k is obtained by averaging adjacent edge tangents and normalizing. Using this tangent, projection operators parallel and perpendicular to the rod are defined as

$$\mathbf{P}_t = \mathbf{t}_k \mathbf{t}_k^\top \quad \mathbf{P}_n = \mathbf{I} - \mathbf{P}_t \quad (21)$$

The resistive force matrix at each node is then given by:

$$\mathbf{M}_k = C_t \mathbf{P}_t + C_p \mathbf{P}_n, \quad (22)$$

where C_t and C_p are the tangential and normal drag coefficients, respectively. The hydrodynamic force acting on node k is computed as:

$$\mathbf{F}_{h,k} = -\ell_k \mathbf{M}_k \mathbf{u}_{\text{rel},k} \quad (23)$$

where ℓ_k denotes the Voronoi length associated with node k . This formulation captures the anisotropic viscous drag experienced by slender structures at low Reynolds numbers.

2) *High Reynolds Number Environment*: At higher Reynolds numbers, inertial effects become significant and the hydrodynamic forces are no longer linearly proportional to velocity. In this regime, a quadratic drag model is employed to represent pressure-dominated loading on the rod.

The relative velocity and its magnitude are defined as [10]:

$$\mathbf{u}_{\text{rel},k} = \mathbf{u}_k - \mathbf{u}_f \quad \|\mathbf{u}_{\text{rel},k}\| = \sqrt{\mathbf{u}_{\text{rel},k}^\top \mathbf{u}_{\text{rel},k}} \quad (24)$$

and the local Reynolds number is computed using the rod diameter $D = 2r_{\text{outer}}$

$$\text{Re}_k = \frac{\|\mathbf{u}_{\text{rel},k}\| D}{\nu} \quad (25)$$

where ν is the kinematic viscosity of seawater, which is assumed to be constant and set to 1×10^{-3} in this study.

The drag coefficient $C_d(\text{Re}_k)$ is obtained from an empirical Reynolds-number-dependent relation for a circular cylinder. The projected area associated with node k is given by

$$A_k = 2r_0\ell_k, \quad (26)$$

and the resulting hydrodynamic drag force is computed as

$$\mathbf{F}_{h,k} = -\frac{1}{2}\rho C_d A_k \|\mathbf{u}_{\text{rel},k}\| \mathbf{u}_{\text{rel},k}, \quad (27)$$

where ρ denotes the fluid density, which is 1025 kg/m^3 for seawater.

3) *Gust Disturbance Modeling*: To evaluate the response of the soft robotic manipulator under unsteady flow conditions, transient gust disturbances are introduced into the background fluid velocity field. Oceanographic data show that currents operate on the order of centimeters per second and with sudden changes move to a few meters per second [11]. The gust is modeled as a time-varying perturbation superimposed on a steady background flow, allowing the simulation to capture sudden changes in hydrodynamic loading that commonly occur in real underwater environments due to waves, currents, or turbulence.

The total background flow velocity is defined as

$$\mathbf{u}_f(t) = \mathbf{u}_{\text{bg}} + \mathbf{u}_{\text{gust}}(t) \quad (28)$$

where \mathbf{u}_{bg} denotes the constant background flow and $\mathbf{u}_{\text{gust}}(t)$ represents the transient gust contribution.

The gust velocity is prescribed using a Gaussian temporal profile,

$$\mathbf{u}_{\text{gust}}(t) = A \frac{1}{\sqrt{2\pi\sigma^2}} \exp\left(-\frac{(t-\mu)^2}{2\sigma^2}\right) \mathbf{d} \quad (29)$$

where A is the maximum gust amplitude, \mathbf{d} is a unit vector defining the gust direction, and the parameters:

$$\sigma = \frac{T_{\text{gust}}}{6} \quad \mu = t_{\text{start}} + \frac{T_{\text{gust}}}{2} \quad (30)$$

control the temporal spread and peak timing of the gust, respectively. Here, t_{start} denotes the gust onset time and T_{gust} is the gust duration.

This Gaussian formulation ensures a smooth onset and decay of the gust, avoiding numerical discontinuities while approximating realistic transient flow disturbances. By applying the gust uniformly across the simulation domain, the resulting hydrodynamic forces directly influence the relative velocity between the rod and the surrounding fluid in both low and high Reynolds number regimes. This approach enables the assessment of the rod's passive dynamic response and the controller's ability to maintain end-effector tracking performance under sudden and time-localized flow perturbations.

V. RESULTS

To evaluate the performance and robustness of the proposed control strategy under hydrodynamic disturbances, two sets of numerical experiments are conducted. All simulations in this section employ the same PID controller applied to the base node in the y -direction, with controller gains set to

$$K_p = 1, \quad K_i = 0.03, \quad K_d = 0.1. \quad (31)$$

A steady background flow of $\mathbf{u}_{\text{bg}} = (0, 0.5) \text{ m/s}$ is applied in all cases. Transient gust disturbances are superimposed on this background flow to evaluate system response under varying flow conditions in a high Reynolds number regime.

A. Effect of Gust Direction

TABLE I: Steady-state end-node tracking errors under different gust directions.

Gust Direction	X Error (m)	Y Error (m)
Positive y	0.008067	0.015856
Negative y	0.008066	0.015338
Southwest	0.008067	0.015357
Northwest	0.008066	0.015844
Southeast	0.008067	0.015275
Northeast	0.008066	0.015830

Table I reports the steady-state tracking errors of the rod's end node under different gust directions in a high Reynolds number environment. Across all tested cases, the steady-state error in the x -direction remains nearly constant, indicating that lateral deformation is primarily governed by unactuated axial dynamics rather than the direction of the imposed gust. Similarly, variations in the y -direction error are relatively small but more pronounced than those observed in the x -direction. Gusts with positive y -components result in slightly larger vertical tracking errors, reflecting the increased hydrodynamic loading due to the background flow acting in the positive y -direction at a magnitude of 0.5 m/s .

Despite these disturbances, the PID controller maintains consistent performance across all tested gust directions, demonstrating robustness to directional flow variations while simultaneously highlighting the inherent limitations of single-axis base actuation.

B. Effect of Gust Amplitude

To further evaluate the robustness of the proposed control strategy, a second set of simulations investigates the effect of varying gust amplitude under high Reynolds number flow

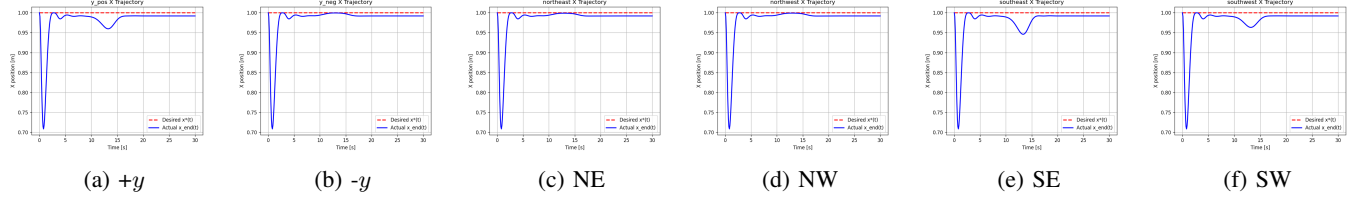


Fig. 4: x trajectories under different gust directions

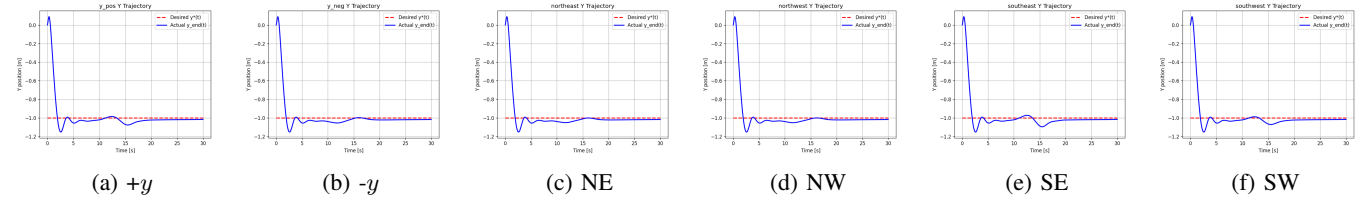
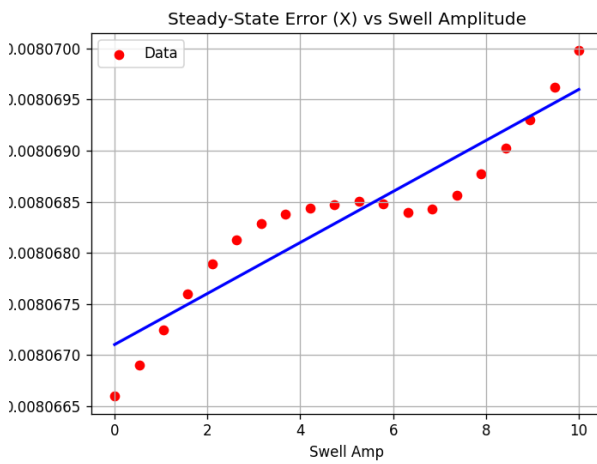
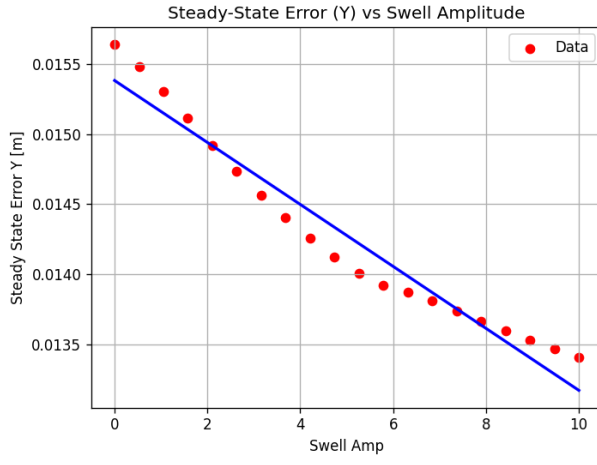


Fig. 5: y trajectories under different gust directions



(a) Steady-state error in the x -direction



(b) Steady-state error in the y -direction

Fig. 6: Effect of gust amplitude on steady-state tracking error of the rod end node under high Reynolds number flow.

conditions. In this study, the gust amplitude is varied over the range

$$A_{\text{swell}} \in [0, 10] \text{ m/s} \quad (32)$$

with 20 steps while the background flow, gust duration, and controller gains remain unchanged. The PID controller is applied only at the base node in the y -direction.

Figure 6 shows the steady-state tracking error of the rod end node in both the x - and y -directions as a function of gust amplitude. The error in the x -direction exhibits a slight increasing trend as the gust amplitude increases. This behavior is attributed to increased axial deformation and compression induced by stronger hydrodynamic loading, which cannot be compensated by the single-axis base actuation strategy.

In contrast, the y -direction steady-state error decreases with increasing gust amplitude. This trend suggests that larger hydrodynamic forces introduce additional effective damping in the transverse direction, allowing the PID controller to more effectively suppress oscillations and reduce steady-state error. Overall, these results highlight the coupled interaction between hydrodynamic forces and structural dynamics, while emphasizing the inherent limitation of controlling the rod using only base actuation in one direction.

VI. CONCLUSION AND FUTURE WORK

The first step moving forward is to improve the convergence properties of the simulation and implement explicit control in the x -direction. While the current controller regulates motion primarily along the y -axis, adding actuation or corrective feedback in the horizontal direction will be essential for accurately stabilizing the appendage, particularly in environments where deformation prevents passive convergence.

The simulation will expand to three dimensions, introducing gravity and buoyancy along the z -axis. In 3D, non-uniform currents will induce twisting and out-of-plane deformation

along the appendage, requiring an additional degree of freedom for full maneuverability. The planned approach is to introduce a revolute joint in the x -direction between the existing linear and revolute joints, enabling a spherical workspace that can be translated through the linear actuator.

Finally, once stability is achieved under these additions, the system will be extended to explore alternative control schemes and more advanced end-effector manipulation strategies. While the current work models a soft appendage mounted on a mobile base, a true soft robotic manipulator would require distributed deformation control along its full length. Although this represents the most complex enhancement to the framework, it is expected to provide the greatest improvement in precision, robustness, and stabilization capability.

REFERENCES

- [1] T. Burch, J. P. Lathrop, W. L. Scott, and D. A. Paley, “Feedback control of a soft swinging appendage,” in *2020 3rd IEEE International Conference on Soft Robotics (RoboSoft)*, pp. 1–6, 2020.
- [2] W. Scott, P. Prakash, and D. Paley, *Distributed Control of a Planar Discrete Elastic Rod for Eel-Inspired Underwater Locomotion*, pp. 261–279. Springer Cham, 01 2021.
- [3] B. Phillips, K. Becker, S. Kurumaya, K. Galloway, G. Whittredge, D. Vogt, C. Teeple, M. Rosen, V. Pieribone, D. Gruber, and R. Wood, “A dexterous, glove-based teleoperable low-power soft robotic arm for delicate deep-sea biological exploration,” *Scientific Reports*, vol. 8, 10 2018.
- [4] Z. Shen, H. Zhong, E. Xu, R. Zhang, K. C. Yip, L. Chan, L. Chan, J. Pan, W. Wang, and Z. Wang, “An underwater robotic manipulator with soft bladders and compact depth-independent actuation,” *Soft Robotics*, vol. 7, 02 2020.
- [5] D. Tong, A. Choi, L. Qin, W. Huang, J. Joo, and K. Jawed, “Sim2real neural controllers for physics-based robotic deployment of deformable linear objects,” *The International Journal of Robotics Research*, vol. 43, 11 2023.
- [6] D. Herrero-Pérez and H. Martínez-Barberá, “Soft gripper design and fabrication for underwater grasping,” *Applied Sciences*, vol. 12, no. 21, p. 10694, 2022.
- [7] I. Smooth-On, “Ecoflex™ 00-30.” Smooth-On website. Accessed: 2025-12-01.
- [8] BASF 3D Printing Solutions BV, “Ultrafuse® TPU 95A Technical Data Sheet.” <https://move.forward-am.com/hubfs/AES> Includes filament properties such as density (1149 kg/m³), Young’s modulus \sim 48.4 MPa, high elongation and impact resistance. Accessed: 2025-01-XX.
- [9] M. H. Sharqawy, J. H. Lienhard, and S. M. Zubair, “Thermophysical properties of seawater: A review of existing correlations and data,” *Desalination*, vol. 390, pp. 1–24, 2010. Viscosity of seawater reported as approximately 1.0×10^{-3} Pa·s at 25 °C.
- [10] M. K. Jawed, “Discrete simulation of slender structures,” 2025. Lecture notes, University of California, Los Angeles.
- [11] T. Bralower and D. M. Bice, “Other deep water masses.” EARTH 103: Earth in the Future. Penn State E-Education website. Accessed: 2025-12-01.